This publication can be referenced as

Grossman-Ponemon, B. E., Heimisson, E. R., Lew, A. J., & Segall, P.. (2020). Logarithmic growth of dikes from a depressurizing magma chamber. *Geophysical Research Letters*, 47, e2019GL086230. https://doi.org/10.1029/2019GL086230

Logarithmic growth of dikes from a depressurizing magma chamber

Benjamin E. Grossman-Ponemon[1], Elías R. Heimisson[2*], Adrian J. Lew[1,3], and Paul Segall[2]

[1]Department of Mechanical Engineering, Stanford University, Stanford, California
[2]Department of Geophysics, Stanford University, Stanford, California, USA
[3]Institute for Computational and Mathematical Engineering, Stanford University, Stanford, California, USA,

Key Points:

- Fully coupled simulations of dike growth and magma chamber depressurization are performed.
- A simple model for dike length with time is identified, and compared to seismic observations.
- A simple model of chamber pressure versus dike length is derived and compared to simulations.

*Now at: Seismological Laboratory, California Institute of Technology

Corresponding author: Benjamin E. Grossman-Ponemon, `bponemon@stanford.edu`

Corresponding author: Elías R. Heimisson, `eliasrh@stanford.edu`

Abstract

Dike propagation is an intrinsically multiphase problem, where deformation and fluid flow are intricately coupled in a fracture process. Here we perform the first fully-coupled simulations of dike propagation in two dimensions, accounting for depressurization of a circular magma chamber, dynamic fluid flow, fracture formation, and elastic deformation. Despite the complexity of the governing equations we observe that the lengthening is well explained by a simple model $a(t) = c_1 \log(1+t/c_2)$, where a is the dike length, t is time, and c_1 and c_2 are constants. We compare the model to seismic data from 8 dikes in Iceland and Ethiopia and, in spite of the assumption of plane strain, we find good agreement between the data and the model. In addition, we derive an approximate model for the depressurization of the chamber with the dike length. These models may help forecast the growth of lateral dikes and magma chamber depressurization.

Plain Language Summary

Volcanic dike intrusions, propagating magma filled fractures, precede most eruptions. Dike propagation has been studied for decades through simplified analytical and numerical models. To date, no study has fully addressed how the fluid magma, host rock, and the magma chamber all interact at the same time and drive the dike forward. We present such simulations for a two-dimensional configuration and deduce that a simple formula can explain how the dike lengthens with time. We suggest that this simple formula may be used to forecast dike growth.

1 Introduction

Modeling of dike propagation has remained a topic of active research to this day since the seminal work of Anderson (1937, 1951), yet many modeling challenges remain unsolved (Rivalta et al., 2015). One is computationally and theoretically rigorous modeling of the fully coupled system, which includes fluid flow, host rock deformation, fracture formation, and depressurization of a magma chamber. Many studies that couple fluid flow and elastic deformation make the simplifying approximation that dike opening is proportional to the local fluid pressure (Pinel & Jaupart, 2000; Pinel et al., 2017), which is not generally valid. Other studies have treated fluid flow and elastic coupling more rigorously for straight dikes (e.g. Lister & Kerr, 1991; Rubin, 1995). However, these studies have not explored the coupling of the dike to the magma chamber through mass exchange and elastic stress transfer. As a result, the space-time behavior of laterally propagating dikes and their coupling to a magma chamber are not fully understood. Laterally propagating dikes are the most commonly observed in field studies (Townsend et al., 2017) and thus understanding their dynamics and emplacement is of great importance to the interpretation of field observations as well as to volcano monitoring and hazard mitigation. New oceanic crust on earth, and perhaps other planets, is primarily generated by dike injections (Wright et al., 2012). Thus, dike dynamics play an important role in the evolution of the crust and lithosphere on a global scale. As the mathematical model of dike propagation from a magma chamber resembles the early-time growth of a hydraulic fracture from a pressurized wellbore, similar problems have been of interest in the hydraulic fracturing community (e.g., Detournay & Carbonell, 1997; D. Garagash & Detournay, 1997; Bunger et al., 2010).

Dike propagation is typically associated with migrating seismic swarms. The advancing front of the swarm coincides approximately with the dike tip location (section 3.3). Thus, the migration speed of the seismic swarm represents the dike propagation speed, and earthquake epicenters delineate the dike path and length (e.g. Sigmundsson et al., 2015). Persistent normal faulting above the dike may accompany the intrusion (Belachew et al., 2012), which does not necessarily map the dike tip. As a crustal dike grows it removes magma from the magma chamber, thereby dropping the chamber pressure and decreasing the chamber volume. The volume change can often be inferred from geodetic measurements.

Our contribution to this problem is twofold. First, we apply a finite element-based method (Grossman-Ponemon & Lew, 2019) to simulate the fully coupled hydraulic fracture problem in two dimensions. Although the method can be used to simulate curvilinear trajectories, for simplicity we restrict our attention to straight propagation. Straight dike propagation is usually appropriate for rift-zone volcanism such as in Iceland, Ethiopia, and Hawaii. Second, we use the simulation results as a guide to establish simplified expressions relating the chamber pressure in and dike length, and the dike length and time. These simplified models provide insight into the important mechanisms driving the evolution of the problem.

2 Mathematical Model

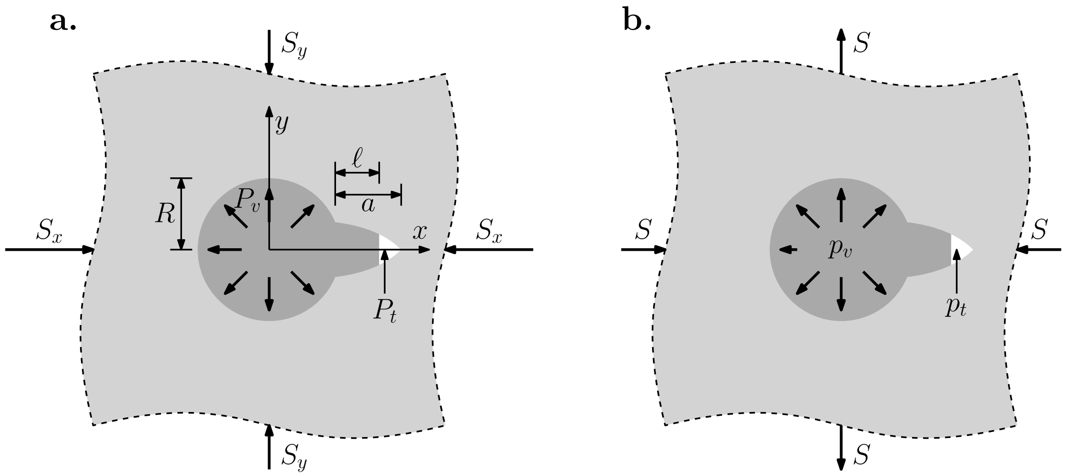

Figure 1. (a) Plan-form view of the radial dike problem, with relevant dimensions and pressures labeled (see text). (b) Problem with mean stress $M = (S_x + S_y)/2$ subtracted. In both figures, the dike is depicted with exaggerated opening.

We model a magma chamber as a circular cavity of radius R and time-varying pressure $P_v(t)$. We assume plane strain deformation and an infinite, isotropic, linear elastic rock with shear modulus μ, Poisson's ratio ν, and fracture toughness K_{Ic}. The storage of magma in the chamber is characterized by the constant $\beta := \rho_m^{-1}\mathrm{d}\rho_m/\mathrm{d}P_v + V_c^{-1}\mathrm{d}V_c/\mathrm{d}P_v$, where $\rho_m(P_v)$ and $V_c(P_v)$ are the (assumed spatially-uniform) magma density in the chamber and the chamber volume, respectively (Rivalta, 2010). We call β the total compressibility. The rock is loaded in the far-field via *in situ* stresses. We align the x and y axes with the principal stresses S_x and S_y, respectively, and we assume $S_x \geq S_y$ (with compression positive). Opening against the minimum stress is a dike of length $a(t)$, partially filled to length $\ell(t)$ by magma. The dike propagates quasi-statically. Within the dike, we model the flow of magma with Reynolds lubrication theory, treating it as an incompressible, laminar, Newtonian fluid with viscosity η. Thus, the compressibility of the magma is accounted for inside the chamber, but not within the dike. In the unimpinged or unwetted portion of the dike, which we call the dike tip cavity, we assume that the exsolved gases and fluids from the magma and host rock produce a pressure $P_t \leq P_v(t)$ (cf. Rubin, 1993b).

The governing equations of the above system are similar to those of linear elastic, hydraulic fracturing problems in the literature (e.g., D. I. Garagash, 2006; Detournay, 2016). Changes to the boundary conditions arise due to the coupling between the dike and the magma chamber (see supporting information).

We subtract the mean stress $M = (S_x + S_y)/2$ without altering the problem (cf. Mériaux & Lister, 2002). The resulting chamber overpressure is $p_v(t) = P_v(t) - M$, the tip underpressure is $p_t = P_t - M$, and the rock is loaded by the far field stress deviator $S = (S_x - S_y)/2$. Henceforth, we will term these quantities chamber pressure, tip pressure, and deviatoric stress, respectively. We introduce the following characteristic length (a_c), stress/pressure (p_c), displacement/dike aperture (w_c), and time (t_c):

$$a_c = R, \quad p_c = S, \quad w_c = \frac{RS}{\mu}, \quad t_c = \frac{\eta\mu^2}{S^3}, \tag{1}$$

where t_c represents a characteristic timescale for magma flow within the dike. If the chamber radius is of order 1 km, the magma viscosity 100 Pa $\cdot$ s (Wada, 1994), the shear modulus 10 GPa, and deviatoric stress 1 MPa (Jónsson, 2012), then the characteristic aperture and time are $w_c = 0.1$ m and $t_c = 10,000$ s, respectively. The latter, being approximately 3 hours, is reasonable given observed duration of diking events. We normalize all relevant quantities by these characteristic dimensions. To differentiate the non-dimensionalized quantities, we use the $\tilde{}$ symbol (e.g. $\tilde{p}$ versus p).

When we non-dimensionalize the problem using (1), four dimensionless parameters arise in the governing equations in addition to Poisson's ratio ν. These are related to the toughness of the rock, the compressibility, the tip pressure, and the initial chamber pressure. Respectively, we denote these

$$\mathcal{K} = \frac{K_{Ic}}{SR^{1/2}}, \quad \mathcal{B} = \beta\mu, \quad \mathcal{T} = \frac{p_t}{S}, \quad \mathcal{P} = \frac{p_v(0)}{S}. \tag{2}$$

By our choice of t_c, the viscosity of the magma drops out of the governing equations. Additionally, the ratio $\tilde{a} = a/R$ is important in the elasticity kernels, behaving similarly to the length versus depth parameter of a near-surface hydraulic fracture (Zhang et al., 2005).

For a circular hole, $V_c^{-1}\mathrm{d}V_c/\mathrm{d}P_v = 1/\mu$, and hence $\mathcal{B} = \mu\beta \geq 1$. The case $\mathcal{B} =$ 1 corresponds to incompressible magma (i.e. $\rho_m^{-1}\mathrm{d}\rho_m/\mathrm{d}P_v = 0$). Meanwhile, we generally expect the parameter $\mathcal{T}$ to fall in the range $[-M/S, -1]$. If a vacuum exists in the dike tip cavity, then $\mathcal{T} = -M/S$. The case $\mathcal{T} = -1$ corresponds to the tip pressure equilibrating with the deviatoric stress (equivalently, the net pressure in the dike tip cavity P_t equals the minimum *in situ* stress $S_y = M - S$). If the tip pressure were larger, the dike would grow unstably (see supporting information).

There is uncertainty in the appropriate values for fracture toughness, with laboratory measurements between roughly 0.1 and 10 $\text{MPa} \cdot \text{m}^{1/2}$ (Atkinson & Meredith, 1987). However, field studies of dike process zones suggest the fracture toughness may be two or three orders of magnitude larger (Delaney et al., 1986), suggesting that a value of 100 $\text{MPa} \cdot \text{m}^{1/2}$ maybe more likely (see Townsend et al. (2017)). Based on previous estimates for the chamber radius and deviatoric stress, we expect $\mathcal{K}$ between 0.003 and 3, with the larger value corresponding to estimates based on dike process zones.

Based on the scale of dikes observed in nature, we are interested in parameter combinations for which $\tilde{a}$ is approximately between 10^{-1} and 10^{1}, where we believe our model to be most applicable (i.e., dikes with length between 100 m and 10 km for a chamber radius of order 1 km). For smaller lengths, thermal and viscous effects, and preexisting cracks are necessary to study how dikes nucleate. When the dike is long and propagation speed becomes small then solidification of the magma becomes important due to decreased flow rate (Rubin, 1993a).

3 Simulation Results and Simplified Models

Next, we describe the results of the fully coupled simulations. In analyzing the results, we explored simple relations that can explain the observed time-dependence of the system.

Within the $\{\mathcal{K}, \mathcal{B}, \mathcal{P}, \mathcal{T}\}$-parameter space, we investigated the behavior of the system under $\mathcal{K} = 3$, the upper end of our expected range, and varying $\mathcal{B} \in \{1, 2, 4, 8, \infty\}$ and $\mathcal{P} \in \{2.5, 5, 10, 20\}$. We selected $\mathcal{T} = -\mathcal{P}$ (i.e. $p_t = -p_v(0)$). One such situation where this occurs is if the tip cavity pressure is zero ($P_t = 0$), while the initial chamber pressure doubles the mean stress ($P_v(0) = 2M$), in which case $\mathcal{T} = -\mathcal{P} = -M$. Poisson's ratio was $\nu = 0.25$.

We chose the scaling of $\{\mathcal{K}, \mathcal{P}, \mathcal{T}\}$ for three reasons (see also supporting information). First, for a given initial dike to be critical ($K_I = K_{Ic}$), increasing $\mathcal{P}$ meant either increasing $\mathcal{K}$ or decreasing $\mathcal{T}$ to balance the increased chamber pressure, and we opted for the latter. Second, for our choice of $\mathcal{K}$, if $\mathcal{T}$ is significantly greater than $-\mathcal{P}$, dikes could become supercritical ($K_I > K_{Ic}$) at early times, implying the crack tip would propagate at speeds comparable to seismic wave speeds. This is unlikely to occur in nature since dike-induced seismic swarms propagate at much lower speed (cf. section 3.3). Lastly, for $\mathcal{T}$ significantly less than $-\mathcal{P}$, the initial dike tip cavity becomes very small with respect to the dike length. Resolving the dike tip cavity at early times is computationally prohibitive.

In the supporting information, we explored the effect of increasing and decreasing $\mathcal{T}$ while keeping the other parameters fixed, and we found that, as long as the dike did not become supercritical, the behavior was largely unaffected by the choice of tip pressure.

The simulations were terminated under one of two conditions: either the dike became too large with respect to the computational domain, or the lag $(a(t) - l(t))$ became equal to the minimum mesh size. For further details of the simulations see the supporting information. In Fig. 2, we show the length of the dike versus time and the pressure in the magma chamber versus dike length for fixed $\mathcal{P} = 10$ and varied $\mathcal{B}$, fixed $\mathcal{B} = 2$ and varied $\mathcal{P}$, and fixed $\mathcal{B} = \infty$ and varied $\mathcal{P}$. The other cases are shown in the supporting information.

3.1 Dike Growth Versus Time

In all cases, the dike length history could be closely represented by the simple relation (cf. dashed curves in Fig. 2)

$$\tilde{a}_{\text{model}}(\tilde{t}) = \dot{a}^* t^* \log(1 + \tilde{t}/t^*), \tag{3}$$

where $\dot{a}^*$ and t^* represent characteristic growth rate and timescale respectively, which we determined by least-squares fitting of the simulated growth. We contrast equation (3) with Rivalta (2010), where an exponential decay of dike velocity based on a quasi-static mass balance between a dike and a chamber was derived. We found exponential decay to be inconsistent with the fully coupled simulations. Equation (3) can be expressed in terms of a characteristic length $a^* = \dot{a}^* t^*$; however, the above definition is favorable because in the limit $t^* \to \infty$, $\tilde{a}_{\text{model}}(\tilde{t}) \to \dot{a}^* \tilde{t}$. This limiting case arises when the magma

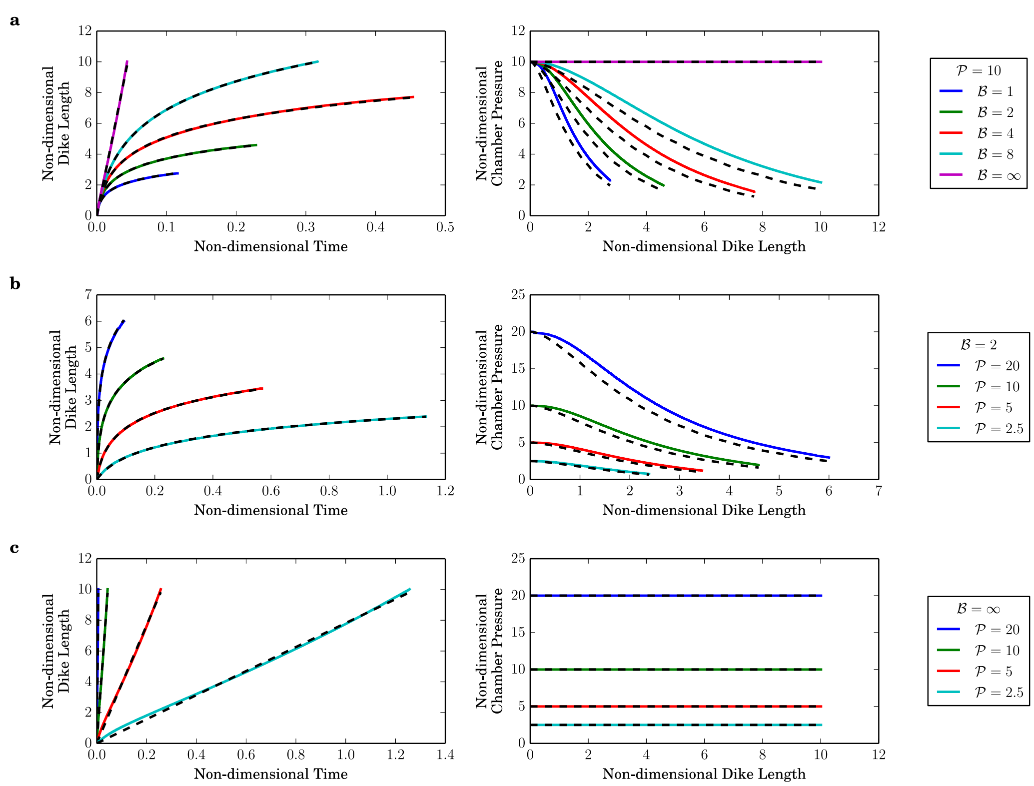

Figure 2. Dike length versus time and chamber pressure versus dike length for (a) $\mathcal{P} = 10$ and varying $\mathcal{B}$, (b) $\mathcal{B} = 2$ and varying $\mathcal{P}$, and (c) $\mathcal{B} = \infty$ and varying $\mathcal{P}$. The fitted model for dike length versus time equation (3) and the simplified pressure versus dike length model equation (5) are shown with black dashed lines.

chamber does not depressurize (i.e. $\mathcal{B} \to \infty$, shown in Fig. 2c) and is explored later. The model above assumes growth starting at $\tilde{t} = 0$. If the dike is initially subcritical then we may shift time by some $\tilde{t}_{\text{start}} > 0$ (see supporting information for details).

The agreement between equation (3) and the simulations is remarkable. In over half of the parameter combinations explored, this simple model could explain more than 99.9% of the variance in the simulated trajectories based on computing an $R^2 = 1 - \chi_{\text{res}}/\chi_{\text{tot}}$ value. The term $\chi_{\text{res}} = \sum_{i=1}^{N} (\tilde{a}(t_i) - \tilde{a}_{\text{model}}(t_i))^2$ is the sum of squares of the residuals between simulations and equation (3), respectively, at each of the N time-steps. Similarly, $\chi_{\text{tot}} = \sum_{i=1}^{N} (\tilde{a}(t_i) - \bar{\tilde{a}})^2$ is the sum of squares of the residuals between simulations and their mean value. All fits had a variance reduction greater than 99.3%. Furthermore, all 20 simulations could be fit simultaneously with a variance reduction of 99.4% using:

$$\dot{a}^* \approx 0.66\mathcal{P}^{2.57^{+0.10}_{-0.14}} \qquad a^* = \dot{a}^* t^* \approx 0.82\mathcal{B}^{0.65^{+0.07}_{-0.07}} \qquad t^* = a^*/\dot{a}^*, \tag{4}$$

where we provided 95% confidence window for the exponents. The confidence bounds were determined by re-sampling the entire simulation time-series with replacement for a set of all 20 simulations and estimating the exponents. The uncertainty thus reflects the range of values that may be found if only a sub-sample of the simulations were available. Exponents $\mathcal{P}^{2.57}$ and $\mathcal{B}^{0.65}$ corresponded to fitting all available simulations. Equation (4) provides insight into how the characteristic time, speed and length vary as compressibility and/or pressure change.

In Fig. 3a, we show $\tilde{a}$ versus $\tilde{t}$ for each of the simulations with $\mathcal{B} < \infty$. We then show that the curves collapse when we rescale the simulated dike length and time by the least-squares fits for a^* and t^* for each simulation and by using the unified fit of equation (4) in Fig. 3b-c, respectively.

3.2 Chamber Pressure Versus Dike Length

To better understand the chamber pressure versus dike length (Fig. 2, right column), we consider a simplified model based on three assumptions. We neglect the length of the dike tip cavity (i.e. we take $\ell = a$), we assume the magma pressure is uniform throughout the dike and equal to p_v, and we assume the initial dike length is very small

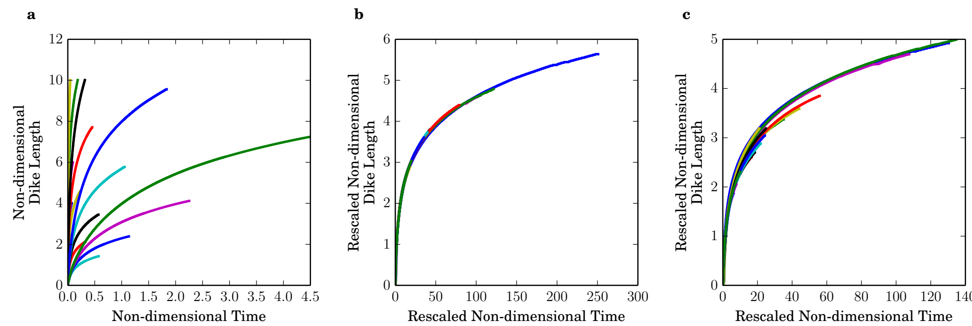

Figure 3. Dike length versus time for all simulations with $\mathcal{B} < \infty$: (a) original data, with length and time normalized as in (1), (b) length and time data rescaled by the least-squares fit for a^* and t^* for each simulation, and (c) length and time data rescaled by the unified fit (4). When rescaled the curves collapse in both cases.

compared to the chamber radius. Under these assumptions, we find (cf. the supporting information)

$$\tilde{p}_{v,\mathrm{model}}(\tilde{a}) = \frac{\pi\mathcal{B}\mathcal{P} - \tilde{v}_S(\tilde{a})}{\pi\mathcal{B} + \tilde{v}_p(\tilde{a})}, \tag{5}$$

where $\tilde{v}_p(\tilde{a})$ and $\tilde{v}_S(\tilde{a})$ denote the non-dimensional crack volume (defined $\tilde{v} = \mu V/R^2$) associated with unit magma pressure and deviatoric stress, respectively. These functions may be computed from the solution of Tweed and Rooke (1973). No closed-form expressions exist for the functions $\tilde{v}_p(\tilde{a})$ and $\tilde{v}_S(\tilde{a})$, plotted in Fig. 4. However, they are well approximated by

$$\tilde{v}_p(\tilde{a}) \approx \tilde{a}^2 \frac{2.96 + \frac{3\pi}{16}\left(\frac{\tilde{a}}{0.636}\right)^{0.915}}{1 + \left(\frac{\tilde{a}}{0.636}\right)^{0.915}} \qquad \tilde{v}_S(\tilde{a}) \approx \tilde{a}^2 \frac{5.92 + \frac{3\pi}{16}\left(\frac{\tilde{a}}{0.369}\right)^{1.03}}{1 + \left(\frac{\tilde{a}}{0.369}\right)^{1.03}} \tag{6}$$

as shown by the black dashed lines in the same figure.

The validity of equation (5) could be tested by using geodetic measurements as a proxy for pressure and migration of seismicity as a proxy for dike length. We leave for future research to identify the appropriate data sets and methodology to make this comparison.

For simulations with $\mathcal{B} < \infty$, the model consistently under-fits the pressure, due to the over-estimate of the magma volume in the dike via neglect of the tip effects. The maximum point-wise discrepancy $\max_{i=1,\ldots,N} |\tilde{p}_v(\tilde{a}_i) - \tilde{p}_{v,\mathrm{model}}(\tilde{a}_i)|$ varied between 6.4%

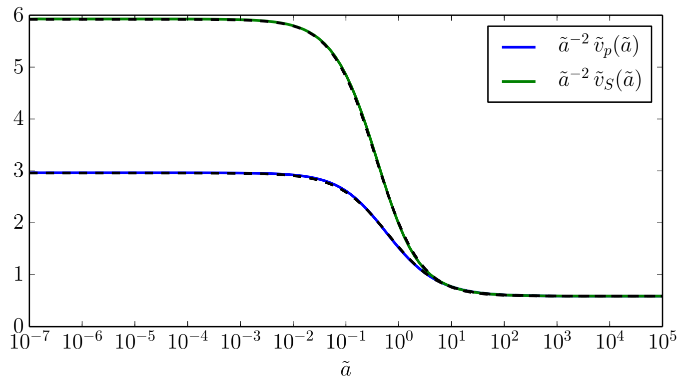

Figure 4. Non-dimensional crack volume functions for a circular hole with a straight edge crack subjected to unit far-field hydrostatic tension (blue curve) and deviatoric stress (green curve), computed using the elasticity solution of Tweed and Rooke (1973). Black dashed lines correspond to the approximations (6). For $\tilde{a} < 10^{-2}$ and $\tilde{a} > 10^{1}$, the elasticity behavior is well approximated by an edge crack and an internal crack with no magma chamber, respectively.

and 11.8% of the initial value $\tilde{p}_v(0)$. The agreement between the model and the full system is remarkable and consistent with the tip region contributing little to the overall mass in the dike. In the supporting information, we present and analyze a second model that accounts for the tip effects.

3.3 Comparison to Seismicity

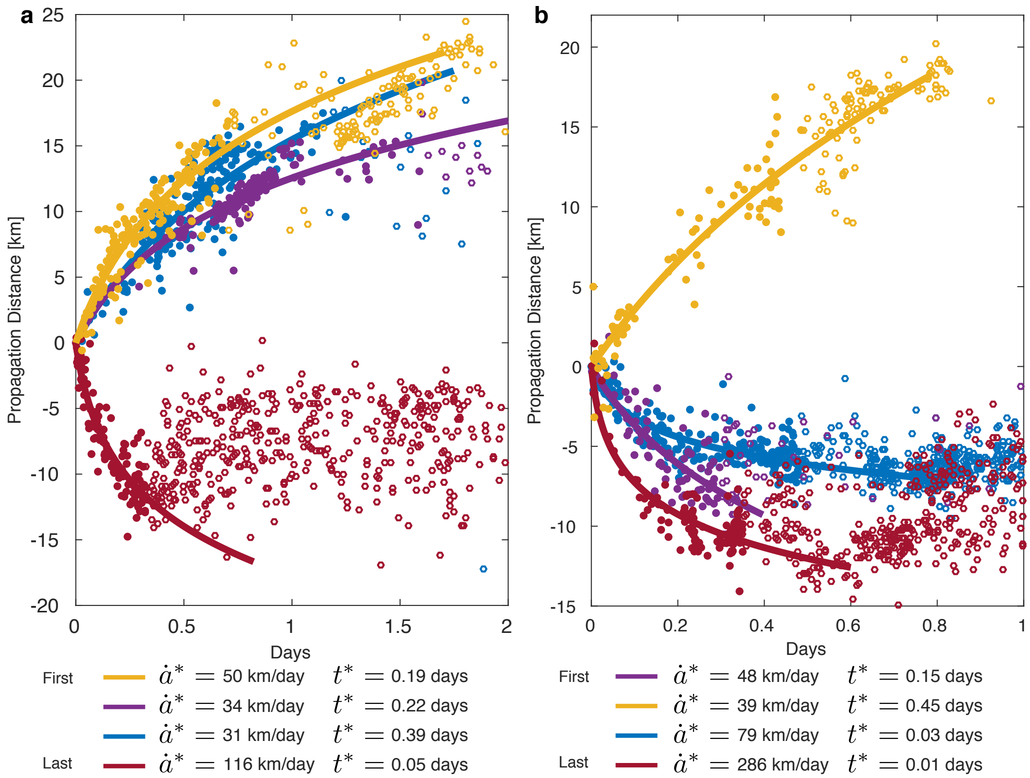

Figure 5. Comparison of equation (3) to four diking events in Afar, Ethiopia (a) and Krafla, Iceland (b). Lines are fits of equation (3) to the seismicity (filled circles). Hollow circles are later seismicity and are not fitted. The lines tend to envelope the hollow circles; suggesting that the model may predict that growth of the dike. In a, blue: July 2008, purple: March 2008, red: October 2008, yellow: November 2007 dikes (Belachew et al., 2011; Tepp et al., 2016) . In b, blue: February 1980, purple: September 1977, red: March 1980, yellow: July 1978 dikes (Einarsson & Brandsdóttir, 1980; Brandsdóttir & Einarsson, 1979). The quantities $\dot{a}^*$ and t^* are reported with dimensions; precise values of the physical parameters needed to non-dimensionalize using a_c and t_c are not known.

A propagating dike typically triggers a propagating swarm of seismicity near the dike tip, which can be inferred from joint interpretation of seismic and geodetic data (Sigmundsson et al., 2015; Heimisson & Segall, 2019). Particularly strong evidence for this relationship was established when the seismic swarm of the September 1977 Krafla dike (purple Fig. 5b) reached the location of a geothermal borehole (Brandsdóttir & Einarsson, 1979) and a small eruption was produced from the borehole (Larsen & Grönvold, 1979), thus directly demonstrating the collocation of the advancing seismicity and magma.

The agreement between equation (3) and the simulations in Fig. 2 suggests that this simple functional form for how dikes grow may be robust and relatively invariant of the details of the system. In order to test this hypothesis, we compared equation (3) to the time evolution of swarms of seismicity triggered by propagating dikes (Fig. 5). We observe agreement between the log model and the seismicity data in Fig. 5, which provides observational support for equation (3). The fitting in Fig. 5 used only a part of the earthquake locations (filled circles). However, the model still followed the advancement of later events (hollow circles), thus indicating potential forecasting capabilities. We suggest that (3) and (5) could be used together or separately to forecast the time evolution of dike propagation and chamber depressurization.

To make the comparison in Fig. 5 between equation (3) to the propagating seismicity recorded during diking events in Iceland and Ethiopia we collected catalogs from the Dabbahu-Manda Hararo rift in Afar, Ethiopia (Belachew et al., 2011; Tepp et al., 2016) and the Krafla rifting episode, Iceland (Einarsson & Brandsdóttir, 1980; Brandsdóttir & Einarsson, 1979). We limited attention to large dikes that showed clear migration of seismicity with time, which resulted in four dikes from each rifting episode being selected for the analysis. Each event was projected onto the nearest point on a line fit through the entire swarm. We then computed the distance from the average location of the first events. We selected $1-5$ events to determine this location, depending on the number of recorded events at the initial stages of the swarm before clear signs of migration occur). We fit (3) to the migration distance of the filled symbols in Fig. 5. The fitting was done by minimizing an L_1 norm in order to decrease the influence of outliers.

4 Discussion

We performed fully coupled simulations of a dike propagating laterally away from a magma chamber in two-dimensions that resolves the coupling of fluid and solid phases. We identified a simple relationship that indicates that dikes grow approximately with the logarithm of time (3). Further, we attain a simple relationship for how pressure in the magma chamber decreases with the length of the dike (5).

We leave for future research a derivation of (3) or a comparable relationship. Our analysis suggests that the logarithmic growth is a manifestation of an intermediate dike length behavior and cannot be explained by the expected dynamics for very small ($\tilde{a} \ll 1$) or large ($\tilde{a} \gg 1$) dikes compared to the chamber radius. This is evidenced by the non-dimensional crack volumes shown in Fig. 4. When $\tilde{a} < 10^{-2}$ and $\tilde{a} > 10^{1}$, the crack behaves as an edge crack or an internal crack with no magma chamber, respectively.

Remarkably, the logarithmic growth model, inspired by two-dimensional behavior, agrees with three-dimensional seismic observations. We suggest that this result can be used to forecast dike growth and the accompanied depressurization and may provide a new way to jointly interpret seismic and geodetic observations. Moreover, we have presented a methodology which couples numerical simulations and analytical analysis in a unique way. Our methodology provides new insights into a physically complicated system evolving in a transitory regime.

Acknowledgments

E.R.H. was supported by NASA under the NESSF Program - Grant NNX16AO40H. P.S. and E.R.H were supported by NASA ROSES ESI - Grant NNX16AN08G. A.J.L. and B.E.G.P. were supported by NSF CMMI-1662452. B.E.G.P and E.R.H. contributed equally to this work. E.R.H. was responsible for running simulations and B.E.G.P. for code development and implementing the numerical approach. We thank Cynthia Ebinger and an anonymous reviewer for their constructive remarks. All data in this study is shown in Figure 5 and is found in: (Einarsson & Brandsdóttir, 1980; Brandsdóttir & Einarsson, 1979; Belachew et al., 2011; Tepp et al., 2016)

References

Ágústsdóttir, T., Woods, J., Greenfield, T., Green, R. G., White, R. S., Winder, T., ... Soosalu, H. (2016). Strike-slip faulting during the 2014 Bárdarbunga-Holuhraun dike intrusion, central Iceland. *Geophysical Research Letters*, *43*(4), 1495-1503. doi: 10.1002/2015GL067423

Anderson, E. M. (1937). IX.-The dynamics of the formation of cone-sheets, ring-dykes, and caldron-subsidences. *Proceedings of the Royal Society of Edinburgh*, *56*, 128–157. doi: 10.1017/S0370164600014954

Anderson, E. M. (1951). *The dynamics of faulting and dyke formation with applica-*

tions to britain. New York: Hafner Pub. Co.

Atkinson, B. K., & Meredith, P. G. (1987). Experinmental fracture mechanics data for rocks and minerals. In B. K. Atkinson (Ed.), *Fracture mechanics of rock* (p. 477-525). Academic Press, London.

Belachew, M., Ebinger, C., Coté, D., Keir, D., Rowland, J., Hammond, J. O., & Ayele, A. (2011). Comparison of dike intrusions in an incipient seafloor-spreading segment in Afar, Ethiopia: Seismicity perspectives. *Journal of Geophysical Research: Solid Earth*, *116*(B6).

Belachew, M., Ebinger, C., & Coté, D. (2012). Source mechanisms of dike-induced earthquakes in the Dabbahu-Manda Hararo rift segment in Afar, Ethiopia: implications for faulting above dikes. *Geophysical Journal International*, *192*(3), 907-917. doi: 10.1093/gji/ggs076

Brandsdóttir, B., & Einarsson, P. (1979). Seismic activity associated with the September 1977 deflation of the Krafla central volcano in northeastern Iceland. *Journal of Volcanology and Geothermal Research*, *6*(3-4), 197–212. doi: https://doi.org/10.1016/0377-0273(79)90001-5

Bunger, A., Lakirouhani, A., & Detournay, E. (2010). Modelling the effect of injection system compressibility and viscous fluid flow on hydraulic fracture breakdown pressure. In *International symposium on in-situ rock stress* (pp. 59–67).

Delaney, P. T., Pollard, D. D., Ziony, J. I., & McKee, E. H. (1986). Field relations between dikes and joints: Emplacement processes and paleostress analysis. *Journal of Geophysical Research: Solid Earth*, *91*(B5), 4920-4938. doi: 10.1029/JB091iB05p04920

Detournay, E. (2016). Mechanics of hydraulic fractures. *Annual Review of Fluid Mechanics*, *48*(1), 311–339. doi: 10.1146/annurev-fluid-010814-014736

Detournay, E., & Carbonell, R. (1997). Fracture-mechanics analysis of the breakdown process in minifracture or leakoff test. *SPE production & facilities*, *12*(03), 195–199. doi: 10.2118/28076-PA

Einarsson, P., & Brandsdóttir, B. (1980). Seismological evidence for lateral magma intrusion during the july 1978 deflation of the Krafla volcano in NE-Iceland. *Journal of Geophysics*, *47*(1), 160–165. Retrieved from `https://journal.geophysicsjournal.com/JofG/article/view/134`

Garagash, D., & Detournay, E. (1997). An analysis of the influence of the pressurization rate on the borehole breakdown pressure. *International journal of solids and structures*, *34*(24), 3099–3118. doi: https://doi.org/10.1016/S0020-7683(96)00174-6

Garagash, D. I. (2006). Propagation of a plane-strain hydraulic fracture with a fluid lag: Early-time solution. *International Journal of Solids and Structures*, *43*(18), 5811–5835. doi: https://doi.org/10.1016/j.ijsolstr.2005.10.009

Grossman-Ponemon, B. E., & Lew, A. J. (2019). An algorithm for the simulation of curvilinear plane-strain and axisymmetric hydraulic fractures with lag using the universal meshes. *International Journal for Numerical and Analytical Methods in Geomechanics*, *43*(6), 1251–1278. doi: 10.1002/nag.2896

Heimisson, E., & Segall, P. (2019). Fully consistent modeling of dike induced deformation and seismicity: Application to the 2014 Bárðarbunga dike, Iceland. *EarthArXiv*. doi: 10.31223/osf.io/fdv8h

Jónsson, S. (2012). Tensile rock mass strength estimated using InSAR. *Geophysical Research Letters*, *39*(21). doi: 10.1029/2012GL053309

Larsen, G., & Grönvold, K. (1979). Volcanic eruption through a geothermal borehole at Námafjall, Iceland. *Nature*, *278*, 707–710. doi: 10.1038/278707a0

Lister, J. R., & Kerr, R. C. (1991). Fluid-mechanical models of crack propagation and their application to magma transport in dykes. *Journal of Geophysical Research: Solid Earth*, *96*(B6), 10049–10077. doi: 10.1029/91JB00600

Mériaux, C., & Lister, J. R. (2002). Calculation of dike trajectories from volcanic centers. *Journal of Geophysical Research: Solid Earth*, *107*(B4). doi: 10.1029/2001JB000436

Pinel, V., Carrara, A., Maccaferri, F., Rivalta, E., & Corbi, F. (2017). A two-step model for dynamical dike propagation in two dimensions: Application to the July 2001 Etna eruption. *Journal of Geophysical Research: Solid Earth*, *122*(2), 1107–1125. doi: 10.1002/2016JB013630

Pinel, V., & Jaupart, C. (2000). The effect of edifice load on magma ascent beneath a volcano. *Philosophical Transactions of the Royal Society of London A: Mathematical, Physical and Engineering Sciences*, *358*(1770), 1515–1532. doi: 10.1098/rsta.2000.0601

Rivalta, E. (2010). Evidence that coupling to magma chambers controls the volume history and velocity of laterally propagating intrusions. *Journal of Geophysical Research: Solid Earth*, *115*(B7). doi: 10.1029/2009JB006922

Rivalta, E., Taisne, B., Bunger, A., & Katz, R. (2015). A review of mechanical models of dike propagation: Schools of thought, results and future directions. *Tectonophysics*, *638*, 1 - 42. doi: https://doi.org/10.1016/j.tecto.2014.10.003

Rubin, A. M. (1993a). On the thermal viability of dikes leaving magma chambers. *Geophysical Research Letters*, *20*(4), 257-260. doi: 10.1029/92GL02783

Rubin, A. M. (1993b). Tensile fracture of rock at high confining pressure: Implications for dike propagation. *Journal of Geophysical Research: Solid Earth*, *98*(B9), 15919–15935. doi: 10.1029/93JB01391

Rubin, A. M. (1995). Propagation of magma-filled cracks. *Annual Review of Earth and Planetary Sciences*, *23*(1), 287–336. doi: https://doi.org/10.1146/annurev.ea.23.050195.001443

Sigmundsson, F., Hooper, A., Hreinsdottir, S., Vogfjörð, K. S., Ófeigsson, B. G., Heimisson, E. R., ... Eibl, E. P. S. (2015, Jan 08). Segmented lateral dyke growth in a rifting event at Bárðarbunga volcanic system, Iceland. *Nature*, *517*(7533), 191–195. (Letter) doi: 10.1038/nature14111

Tepp, G., Ebinger, C. J., & Yun, S.-H. (2016). Spectral analysis of dike-induced earthquakes in Afar, Ethiopia. *Journal of Geophysical Research: Solid Earth*, *121*(4), 2560–2574. doi: 10.1002/2015JB012658

Townsend, M. R., Pollard, D. D., & Smith, R. P. (2017). Mechanical models for dikes: A third school of thought. *Tectonophysics*, *703*, 98–118. doi: 10.1016/j.tecto.2017.03.008

Tweed, J., & Rooke, D. (1973). The distribution of stress near the tip of a radial crack at the edge of a circular hole. *International Journal of Engineering Science*, *11*(11), 1185–1195. doi: 10.1016/0020-7225(73)90084-0

Wada, Y. (1994). On the relationship between dike width and magma viscosity. *Journal of Geophysical Research: Solid Earth*, *99*(B9), 17743-17755. doi: 10.1029/94JB00929

Wright, T. J., Sigmundsson, F., Pagli, C., Belachew, M., Hamling, I. J., Brandsdóttir, B., ... Ebinger, C. (2012). Geophysical constraints on the dynamics of spreading centres from rifting episodes on land. *Nature Geoscience*, *5*(4), 242. doi: 10.1038/ngeo1428

Zhang, X., Jeffrey, R. G., & Detournay, E. (2005). Propagation of a hydraulic fracture parallel to a free surface. *International Journal for Numerical and Analytical Methods in Geomechanics*, *29*(13), 1317–1340. doi: 10.1002/nag.461

Supporting Information for "Logarithmic growth of dikes from a depressurizing magma chamber"

Benjamin E. Grossman-Ponemon[1], Elías R. Heimisson[2] *, Adrian J. Lew[1,3],

and Paul Segall[2]

[1]Department of Mechanical Engineering, Stanford University, Stanford, California

[2]Department of Geophysics, Stanford University, Stanford, California, USA

[3]Institute for Computational and Mathematical Engineering, Stanford University, Stanford, California, USA,

Contents of this file

1. Text S1 to S4
2. Figures S1 to S7
3. Tables S1 and S2

*Now at: Seismological Laboratory,

California Institute of Technology

Introduction

- Text S1 contains further information on the governing equations and numerical methods used in the main text.
- Text S2 reports simulation results not shown in the main text. This text also briefly explains Supplementary Figures S1 and S2.
- Text S3 provides further details on the effect of the dike tip pressure on propagation.
- Text S4 provides further details on the model for depressurization with dike length.

Text S1.

About the Governing Equations

Here, we comment briefly about the governing equations of the problem described in the main text of this manuscript. A list of variables which appear in the equations may be found in Table S1. At a time t the rock occupies the domain

$$\Omega(t) = \left\{(x,y) \in \mathbb{R}^2 \,|\, x^2 + y^2 > R^2\right\} \setminus \left\{(x,y) \in \mathbb{R}^2 \,|\, R \leq x \leq R + a(t),\, y = 0\right\}.$$

Along with the time-evolving variables $\{p_v(t), a(t), \ell(t)\}$ described in the main text, we also have the displacement field in the rock, $\mathbf{u}(x, y, t)$, defined for any $(x, y) \in \Omega(t)$ and $p(x, t)$ the magma pressure in the dike, defined for any $x \in (R, R + \ell(t))$.

In addition to the equations governing the evolution of a plane-strain hydraulic fracture with lag (not recapitulated here, see Garagash (2006)), there is also the coupled physics of the magma chamber. This enters the problem in three ways. First, the magma chamber adds a boundary condition to the quasi-static elasticity problem. Letting $\sigma(\nabla\mathbf{u}(x, y, t))$ be the Cauchy stress tensor for displacement gradient $\nabla\mathbf{u}$, and $\mathbf{n}$ the outward normal vector, we have

$$\sigma(\nabla\mathbf{u}(x, y, t)) \cdot \mathbf{n}(x, y) = -p_v(t)\mathbf{n}(x, y) \tag{1}$$

whenever $x^2 + y^2 = R^2$. Second, we match the pressure at the dike inlet to that in the magma chamber:

$$p(R,t) = p_v(t). \tag{2}$$

This Dirichlet boundary condition contrasts the volumetric inflow prescribed in the hydraulic fracturing literature (Detournay, 2016). Lastly, we account for the depressurization of the magma chamber. Assuming no additional inflow into the magma chamber, and spatially uniform magma density, the mass balance is given by:

$$\frac{\mathrm{d}p_v(t)}{\mathrm{d}t} = -\frac{1}{\pi R^2 \beta}\left[-\frac{1}{12\eta} w(x,t)^3 \frac{\partial p(x,t)}{\partial x}\right]_{x=R}, \tag{3}$$

with $w(x,t) = u_y(x,0^+,t) - u_y(x,0^-,t))$ being the aperture of the dike. We note that the bracketed quantity is precisely the Poisseuille relation for the volumetric flow rate in a narrow channel.

Numerical Method

We solve the fully coupled problem numerically using the method presented in Grossman-Ponemon and Lew (2019). All simulations were run in a square domain with a domain edge length of $L = 100a_c$. This value was chosen to minimize boundary effects.

Unless otherwise stated, all simulations were initialized with fluid fraction $\ell(0)/a(0) = 0.5$. The initial dike size $a(0)$ was picked by selecting approximately the smallest crack that could become supercritical ($K_I \geq K_{Ic}$) with the given tip pressure and critical fracture toughness. The initial dike sizes ranged from $0.025 - 0.10$ of a_c, where smaller values of $a(0)$ were used with larger values of $\mathcal{P}$.

The edge length of the smallest element in the simulations was kept constant at approximately $a_c/160$. If the lag region became smaller than that, or if the dike propagated further than $10a_c$, the simulations were stopped. The latter requirement was placed to ensure that the dike was not influenced by edge effects.

We now comment on modifications to the algorithm in Grossman-Ponemon and Lew (2019) to account for the depressurization of the volcanic chamber and the pressure boundary condition at the inlet of the dike.

During a timestep, the pressure in the magma chamber was fixed. When the explicit crack propagation steps were completed, the pressure was updated by $(\mathrm{d}p_v/\mathrm{d}t)\Delta t$. We estimated $\mathrm{d}p_v/\mathrm{d}t$ using the pressure gradient and aperture values at the inlet. Meanwhile, the flow rate at the fluid front was calculated using volume conservation along the length of the dike along with the inflow rate.

To prevent the magma from overshooting the tip of the dike, we selected the timestep in the following way. First, given a maximum timestep $\Delta t_{\max}$ and a maximum fluid advancement $\Delta\ell_{\max}$, we selected the timestep $\Delta t^{(1)} = \min\{\Delta t_{\max}, \Delta\ell_{\max}/\dot{\ell}\}$, where $\dot{\ell}$ is the fluid speed averaged over the width of the dike. Then, we selected the smallest non-negative integer n so that $2^{-n}\dot{\ell}\Delta t^{(1)} < a - \ell$, where $a - \ell$ is the size of the lag region. In this way, we had $\Delta t = 2^{-n}\Delta t^{(1)}$

Text S2.

For completeness, we show the dike length versus time and chamber pressure versus dike length results for the entirety of the parametric space studied. In Fig. S1, we show the behavior for fixed $\mathcal{P} \in \{2.5, 5, 20\}$, as we vary $\mathcal{B}$. Meanwhile, in Fig. S2, we vary $\mathcal{P}$, fixing $\mathcal{B} \in \{1, 4, 8\}$. The results for fixed $\mathcal{P} = 10$ and varying $\mathcal{B}$, fixed $\mathcal{B} = 2$ and varying $\mathcal{P}$, and fixed $\mathcal{B} = \infty$ and varying $\mathcal{P}$ are shown in the main text.

Text S3.

In the main text, we restricted our exploration of the $\{\mathcal{K}, \mathcal{B}, \mathcal{P}, \mathcal{T}\}$-parameter space by selecting $\mathcal{T} = -\mathcal{P}$. Physically, this restriction corresponds to the case where the difference between the chamber pressure and the mean stress is equal to the difference between the mean stress and the tip pressure; for example, if the dike tip cavity is in a vacuum and the chamber pressure is twice the mean stress, then $-\mathcal{T} = \mathcal{P} = M$.

In this section, we first discuss how unstable growth arises when the tip pressure is too large to keep the dike stable. Second, we present a numerical investigation into the effect of the tip pressure, starting with one of the cases studied in the main text.

An upper bound on tip pressure

As a starting point for understanding the stability of the system, we remove the magma from the dike, and we only consider the loading from the magma chamber, the far-field stresses, and the tip pressure acting along the entirety of the dike, cf. Fig. S3a. In other words, we assume the dike is fully unwetted. The impingement of magma further opens the dike, increasing the stresses at the dike tip. The unwetted dike may be viewed as the limiting case of the fluid length going to zero ($\ell \to 0$). For very short and very long unwetted dikes (cf. Fig. S3b-c), the stress intensity factor is approximately

$$\frac{K_{I,\text{short}}}{S\sqrt{R}} = (4 + \mathcal{P} + \mathcal{T})\kappa_0 \tilde{a}^{1/2} \text{ and } \frac{K_{I,\text{long}}}{S\sqrt{R}} = (1 + \mathcal{T})\sqrt{\frac{\pi}{2}}\tilde{a}^{1/2},$$

respectively. We can compute the corresponding stress intensity factor for intermediate value of $\tilde{a}$ using the elasticity solution of Tweed and Rooke (2019), as shown in Fig. S3d. We estimated $\kappa_0 \approx 1.988$ from the Tweed and Rooke solution, while the factor $\sqrt{\pi/2}$

comes from the stress intensity factor for a straight crack of length 1 in an infinite domain under unit far-field tension.

In Fig. S3d, we plot the unwetted contribution to the stress intensity factor as a function of the dike length, varying the value of $\mathcal{T}$. We remark that $\mathcal{T} = \mathcal{P}$ is equivalent to the case where pressure is constant along the length of the dike. We observe that if the tip pressure is sufficiently large (e.g. $\mathcal{T} = -1$ or $\mathcal{T} = -5$ in the figure), then there exist dike lengths for which an unwetted crack is supercritical ($K_I > K_{Ic}$). The presence of magma within the dike only further raises the stress intensity factor, meaning that unstable crack growth is unavoidable for sufficiently large values of $\mathcal{T}$.

From a physical standpoint, unstable dike growth is unlikely to occur in natural dikes over significant propagation distances. First, unstable propagation, which is not driven by magma flow, implies that the propagation speed is limited only by inertial effects and rupture would occur at a speed comparable to seismic wave speeds. Second, if the lag region grows at speeds comparable to seismic wave speeds the tip would radiate seismic waves that could be detected on seismometers. In the best monitored large dike intrusion to date, the 2014 Bárdarbunga dike in Iceland, focal mechanism estimations for earthquakes were exclusively double-couple (Agustsdottir et al., 2016), whereas seismic dike opening would produce a characteristic tensile source (a non double-couple) focal mechanism. The focal mechanisms from the Bárdarbunga dike suggest that either such tensile events do not occur or are too small to detect.

Numerical results for varying tip pressure

We now present a study of the effect of varying $\mathcal{T}$. We fixed $\{\mathcal{K}, \mathcal{B}, \mathcal{P}\} = \{3, 2, 10\}$. In addition to $\mathcal{T} = -10$ previously studied in the main text, we also selected $\mathcal{T} \in \{-5, -12, -14, -20\}$. In the short-dike limit, the case $\mathcal{T} = -14 = -4 - \mathcal{P}$ gave $K_{I,\text{short}} = 0$. As seen in Fig. S3, taking $\mathcal{T} = -5$ led to unstable crack propagation. All simulations were initialized to match the $\mathcal{T} = -10$ case in the main text, with with linear pressure profiles occupying the first half of the dike, and $\tilde{a}(0) = 0.05$. We plot the dike length versus time and the chamber pressure versus dike length for varying $\mathcal{T} \in \{-10, -12, -14, -20\}$ in Fig. S4. Varying $\mathcal{T}$ causes only minor changes to the length and pressure evolution. For an interested reader, we will provide some analysis of these secondary effects below.

As we decreased the tip pressure from -10 to -20, we noticed two trends. First, for a given dike length, the chamber pressure also decreased (see right inset in Fig. S4). As the tip pressure was decreased, the dike tip cavity had to shrink in order to remain at equilibrium. This corresponded to a larger amount of magma being injected into the dike and, hence, decreased chamber pressure. Ultimately, if $\mathcal{T} \to -\infty$, we would expect the dike tip cavity to vanish and the pressure profile to approach the fully pressurized distribution.

Second, as we decreased $\mathcal{T}$, we observed slow, early-time growth. This behavior was especially prominent in the $\mathcal{T} = -20$ case (see left inset in Fig. S4). As mentioned previously, when the tip pressure was lowered, a dike of a given length required more magma in order to remain at equilibrium. However, although the magma pressure gradient across the dike increased, the inlet aperture decreased, which negatively impacted the magma volume flowrate into the dike. Hence, more time was required to achieve the larger magma volumes within the dike. As the dike grew larger, the dike tip cavity continued to shrink, and hence its effect was less important.

The net effect of the slow growth behavior was to delay the onset of the logarithmic growth regime; to address this, we shifted the log model from the main text by a start time $\tilde{t}_{\text{start}}$

$$\tilde{a}_{\text{model}}(\tilde{t}) = \dot{a}^* t^* \log\left(1 + \frac{\tilde{t} - \tilde{t}_{\text{start}}}{t^*}\right). \tag{4}$$

For each simulation, we selected $\tilde{t}_{\text{start}}$ as the minimizer of the root-mean-square error of the fitted data points $\{(\tilde{t}_i, \tilde{a}_i)\}_i$ for which $\tilde{t}_i \geq \tilde{t}_{\text{start}}$. The shifted log models are shown as black dashed curves in Fig. S4. In Table S2, we show the computed values for $\dot{a}^*$, t^*, a^*, and $\tilde{t}_{\text{start}}$. For $\mathcal{T} = -10$, $\tilde{t}_{\text{start}}$ was two orders of magnitude smaller than t^*, which meant the unshifted and shifted log models produced nearly the same fit. Meanwhile, for $\mathcal{T} = -20$, the two timescales were on the same order, implying that the slow growth regime could not be neglected.

Interestingly, based on the range of $\mathcal{T}$ studied, a^* was nearly identical across all tip pressures, whereas t^* slightly increased as $\mathcal{T}$ decreased. The time shift was the only parameter to vary significantly, growing by two orders of magnitude when decreasing $\mathcal{T}$ by a factor of 2. Additional simulations at higher tip pressures are necessary to determine if the parameters vary substantially in the limit of $\mathcal{T} \ll 0$.

Finally, we return to the case $\mathcal{T} = -5$, for which we show the dike length versus time and chamber pressure versus dike length in Fig. S5. As we expected from the discussion on stability, the case $\mathcal{T} = -5$ had a range of dike lengths for which an unwetted dike would become unstable. Thus, the dike was initially supercritical ($K_I > K_{Ic}$), growing from $\tilde{a}(0) = 0.05$ to approximately 0.64 in one timestep, which we show in the inset in the same figure.

As a consequence of the initial rapid growth, for a given dike length, the chamber pressure was higher than in the $\mathcal{T} = -10$ case. This trend held true during later growth stages as well. Raising the tip pressure from -10 to -5 meant that the dike tip cavity could be larger, and hence, less magma was needed to keep the dike in equilibrium.

Because of the initial jump in the length of the dike, we did not attempt to fit the simulations with our log model (4). The dike growth does look qualitatively similar to a logarithmic growth in parts of the time-series (Fig. S5). However, the simple log model proposed here can clearly not fit a significant instantaneous jump in length without modifications. Since this regime is unlikely relevant to physical dikes, we entrust further analysis to future study.

Text S4.

Here we present the derivation of two models to relate the pressure within the magma chamber to the length of the dike. In both models, we assume that the dike is always propagating so that there is a one-to-one relationship between a and t. We also assume that the size of the dike tip cavity is very small compared to the length of the dike.

Starting from the depressurization relationship (3), we integrate both sides in time to get the volume balance

$$\pi R^2 \beta (p_v(0) - p_v(t)) = V(t) - V(0), \tag{5}$$

where $V(t)$ is the volume of magma in the dike. Going forward, we will neglect the initial magma volume $V(0)$.

If we assume that the magma pressure is uniform along the length of the dike, the only forces acting on the system are the pressure p_v on the walls of the magma chamber and the faces of the dike and the deviatoric stress S at infinity. Recalling the elasticity solution of Tweed and Rooke (1973), there exist functions V_p and V_S, depending only on a/R, which describe the volume of the crack when acted upon by unit-strength far-field hydrostatic pressure and deviatoric stress, respectively. Hence, we may write $V(t) = p_v(t)V_p(a(t)/R) + SV_S(a(t)/R)$. Thus, rearranging (5), we have an expression for p_v as a function of a:

$$p_v(a) = \frac{\pi R^2 \beta p_v(0) - SV_S(a/R)}{\pi R^2 \beta + V_p(a/R)}.$$

Normalizing by the characteristic dimensions, and defining $\tilde{v}_{p,S} := \mu V_{p,S}/R^2$, we get first the model presented in the main text,

$$\tilde{p}_{v,\text{model}}(\tilde{a}) = \frac{\pi\mathcal{B}\mathcal{P} - \tilde{v}_S(\tilde{a})}{\pi\mathcal{B} + \tilde{v}_p(\tilde{a})} \tag{6}$$

If we relax the assumption that the pressure within the dike is constant, we may expand the fluid volume as $V(t) = p_v(t)V_p(a(t)/R) + SV_S(a(t)/R) + V_{\text{rem}}(t)$. We know that the volume contribution $V_{\text{rem}}(t)$ is caused by the deviation of the magma pressure from the chamber pressure. This deviation varies from 0 at the dike inlet to $p_t - p_v(t)$ at the tip. Hence, we factor out the magnitude of the loading: $V_{\text{rem}}(t) = (p_t - p_v(t))V_t(t)$. Rearranging as before, scaling by characteristic dimensions, and defining $\tilde{v}_t := \mu V_t/R^2$, we arrive at the refined model

$$\tilde{p}^{(1)}_{v,\text{model}}(\tilde{a}) = \frac{\pi\mathcal{B}\mathcal{P} - \tilde{v}_S(\tilde{a}) - \mathcal{T}\tilde{v}_t(\tilde{a})}{\pi\mathcal{B} + \tilde{v}_p(\tilde{a}) - \tilde{v}_t(\tilde{a})} \tag{7}$$

Inspired by the behavior of $\tilde{v}_p(\tilde{a})$ and $\tilde{v}_S(\tilde{a})$, we propose the functional form for $\tilde{v}_t$:

$$\tilde{v}_t(\tilde{a}) = \tilde{a}^2 \frac{C^*}{1 + \left(\frac{\tilde{a}}{A^*}\right)^{\gamma^*}}. \tag{8}$$

This model has two limiting behaviors. For $\tilde{a}/A^* \ll 1$, we have $\tilde{v}_t(\tilde{a}) \approx C^*\tilde{a}^2$. When the dike is very short, we expect the pressure profile within the dike to not vary much in time, yielding approximately self-similar behavior. Meanwhile, as the dike grows, the size of the dike tip cavity shrinks, as the decaying chamber pressure means more of the dike must be filled in order to keep propagating. In (8), this behavior is approximated as $\tilde{v}_t(\tilde{a}) \approx C^*(A^*)^{\gamma^*}\tilde{a}^{2-\gamma^*}$.

In Fig. S6, we plot $\tilde{v}_t(\tilde{a})$ computed for each simulation as well as the best fit using the functional form (8). For cases where $\mathcal{B} < \infty$, (8) provided a reasonable approximation of the tip cavity volume. However, when $\mathcal{B} = \infty$, the approximation broke down. Interestingly in this case, when $\tilde{a}$ is large, we have $\tilde{v}_t(\tilde{a}) \sim \tilde{a}^2$, which is similar to the functions $\tilde{v}_p(\tilde{a})$ and $\tilde{v}_S(\tilde{a})$.

Given the best fits for (8), we compared the models (6) and (7) with the numerical data for $\tilde{p}_v(\tilde{a})$, shown in Fig. S7. Whereas the unfitted model had errors between the 6.4% and 11.8% of the initial pressure, the fitted model deviated from the numerical data by at most 1.4% of the initial pressure.

References

Ágústsdóttir, T., Woods, J., Greenfield, T., Green, R. G., White, R. S., Winder, T., … Soosalu, H. (2016). Strike-slip faulting during the 2014 Bárdarbunga-Holuhraun dike intrusion, central Iceland. *Geophysical Research Letters*, *43*(4), 1495-1503. doi: 10.1002/2015GL067423

Detournay, E. (2016). Mechanics of hydraulic fractures. *Annual Review of Fluid Mechanics*, *48*(1), 311–339. doi: 10.1146/annurev-fluid-010814-014736

Garagash, D. I. (2006). Propagation of a plane-strain hydraulic fracture with a fluid lag: Early-time solution. *International Journal of Solids and Structures*, *43*(18), 5811–5835. doi: https://doi.org/10.1016/j.ijsolstr.2005.10.009

Grossman-Ponemon, B. E., & Lew, A. J. (2019). An algorithm for the simulation of curvilinear plane-strain and axisymmetric hydraulic fractures with lag using the universal meshes. *International Journal for Numerical and Analytical Methods in*

Geomechanics, *43*(6), 1251–1278. doi: 10.1002/nag.2896

Tweed, J., & Rooke, D. (1973). The distribution of stress near the tip of a radial crack at the edge of a circular hole. *International Journal of Engineering Science*, *11*(11), 1185–1195. doi: 10.1016/0020-7225(73)90084-0

Name	Description
$\Omega(t)$	Problem domain
$\mathbf{n}$	Unit outward normal vector to Ω
$a(t)$	Dike length
$\ell(t)$	Length of dike wetted by magma
$p_v(t)$	Magma overpressure in chamber
$\mathbf{u}(x, y, t)$	Displacement field within the rock
$\sigma(\nabla \mathbf{u}(x, y, t))$	Cauchy stress tensor in the rock
$p(x, t)$	Magma pressure along the dike
$w(x, t)$	Aperture along dike
$V(t)$	Volume of magma within the dike
R	Magma chamber radius
p_t	Pressure in the dike tip cavity
S	Far-field deviatoric stress
β	Compressibility of the magma-chamber system
K_{Ic}	Fracture toughness of the rock
μ	Shear modulus of the rock
ν	Poisson's ratio of the rock
η	Viscosity of the magma within the dike

Table S1. Names and descriptions of symbols appearing in the governing equations.

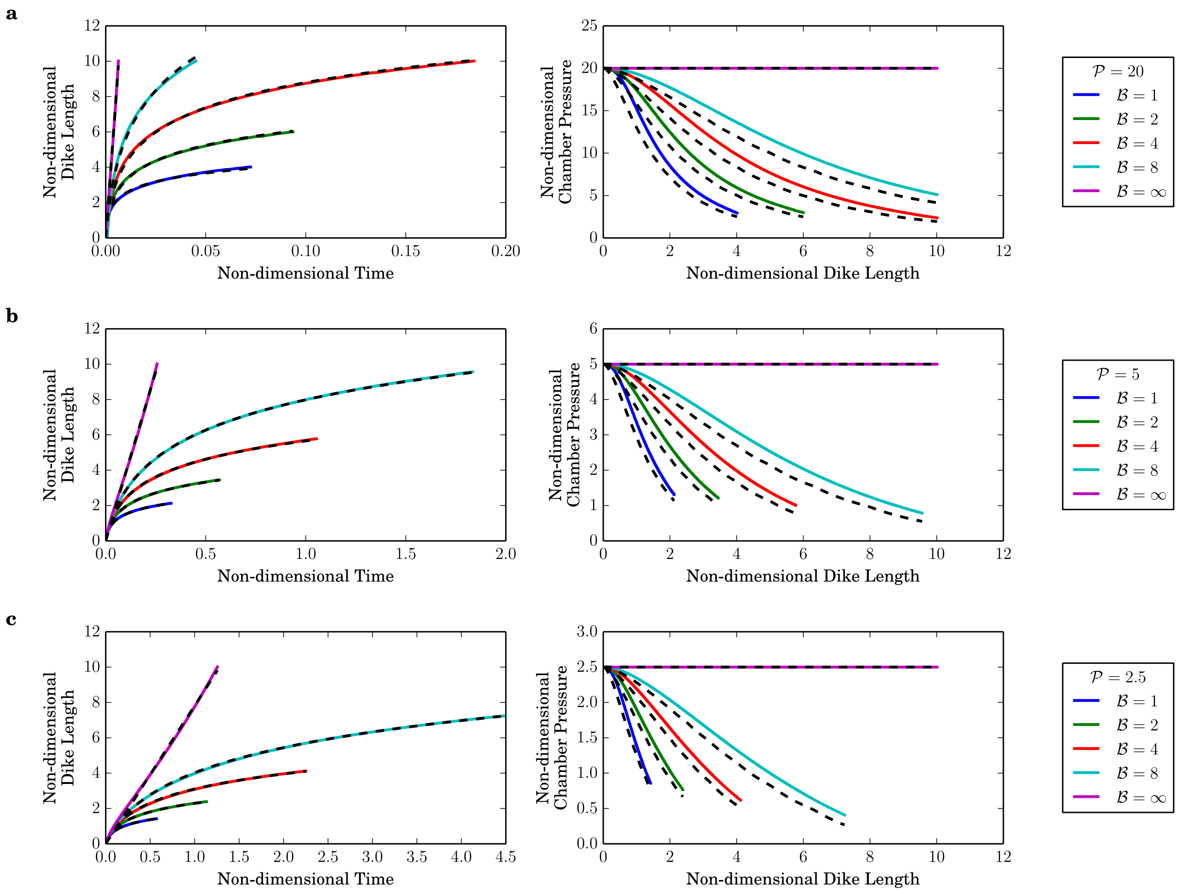

Figure S1. Dike length versus time and chamber pressure versus dike length for (a) $\mathcal{P} = 20$, (b) $\mathcal{P} = 5$, and (c) $\mathcal{P} = 2.5$, varying $\mathcal{B} \in \{1, 2, 4, 8, \infty\}$. The fitted logarithm model for dike length versus time and the simplified pressure versus dike length model are shown with black dashed lines.

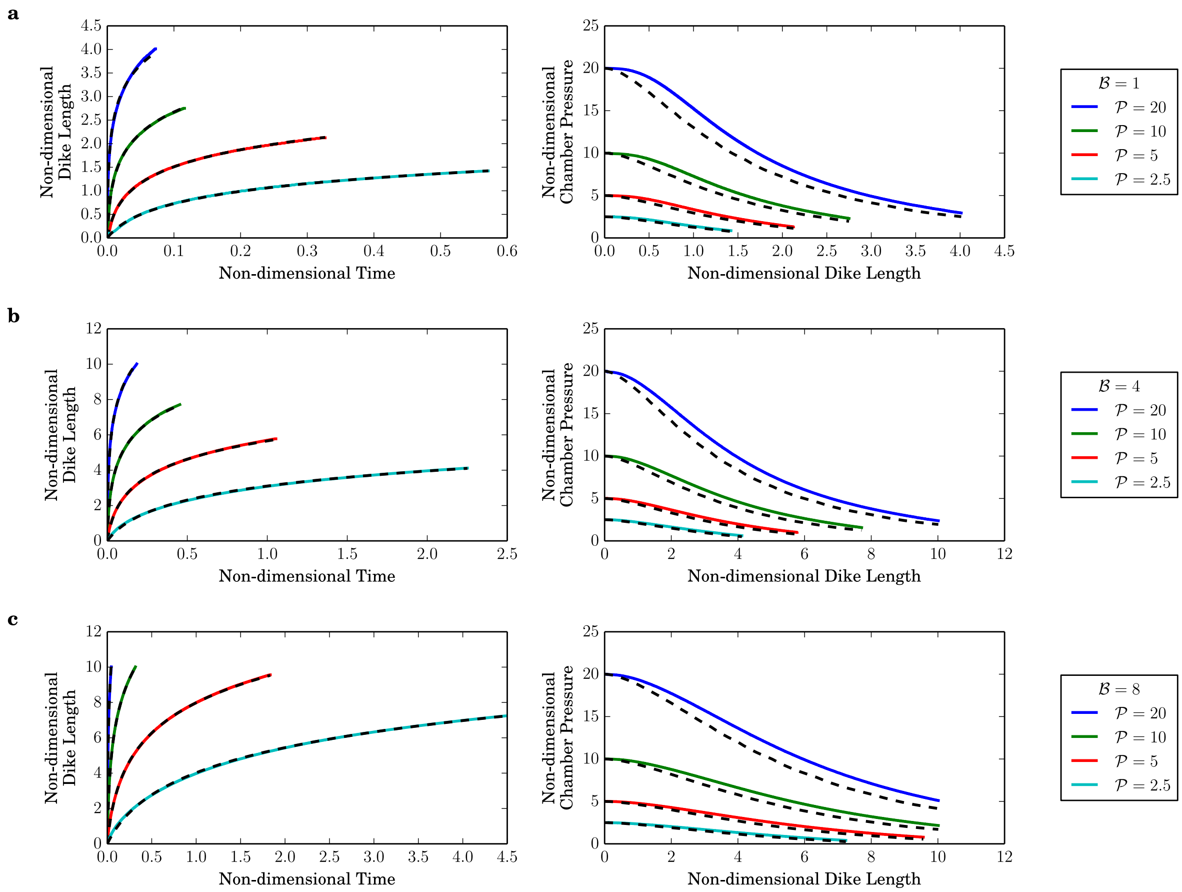

Figure S2. Dike length versus time and chamber pressure versus dike length for (a) $\mathcal{B} = 1$, (b) $\mathcal{B} = 4$, and (c) $\mathcal{B} = 8$, varying $\mathcal{P} \in \{2.5, 5, 10, 20\}$. The fitted logarithm model for dike length versus time and the simplified pressure versus dike length model are shown with black dashed lines.

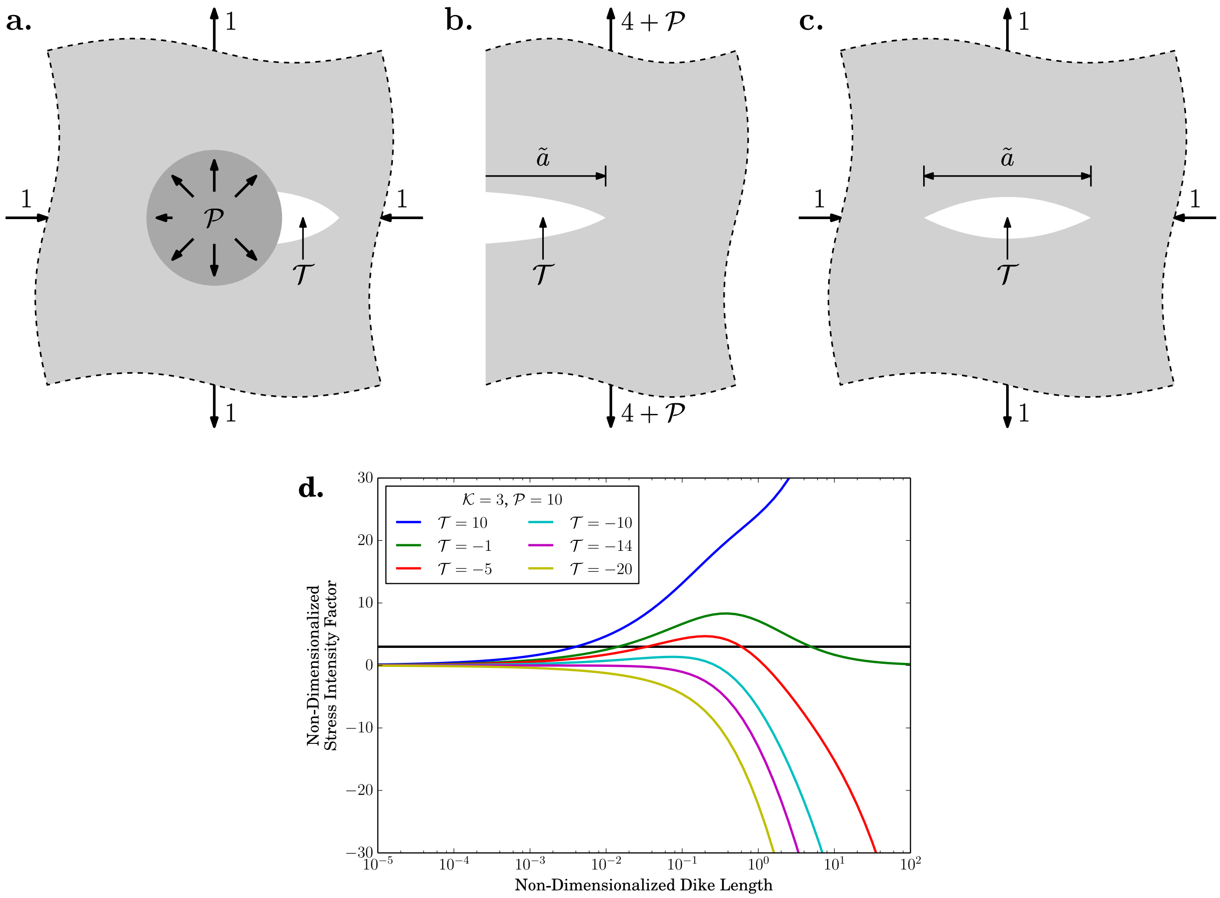

Figure S3. (a) Schematic of the initial configuration of an unwetted dike. The loads applied to the system are the initial chamber pressure, the far-field deviatoric stress, and the tip pressure along the faces of the dike, all of which have been normalized by the deviatoric stress. (b) Approximate geometry and loading for a short, unwetted dike ($\tilde{a} \ll 1$), ignoring the stresses in the horizontal direction. (c) Approximate geometry and loading for a long, unwetted dike ($\tilde{a} \gg 1$). In (a-c), the opening of the dike is exaggerated. (d) Stress intensity factor versus dike length for an unwetted dike for $\mathcal{K} = 3$ and $\mathcal{P} = 10$. The black line indicates $\mathcal{K} = 3$. The case $\mathcal{T} = \mathcal{P} = 10$ (blue line), also applies to when magma is evenly distributed and uniformly pressurized along the length of the dike.

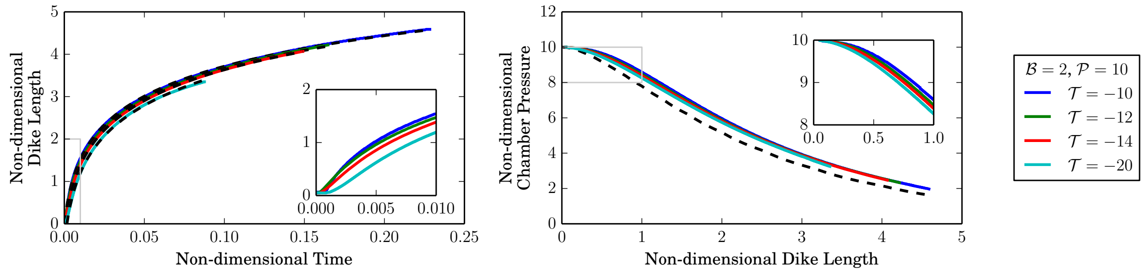

Figure S4. Dike length versus time and chamber pressure versus dike length for $\mathcal{K} = 3$, $\mathcal{B} = 2$, $\mathcal{P} = 10$, and varying $\mathcal{T} \in \{-10, -12, -14, -20\}$. Dashed lines indicate the log model (4) and depressurization model (6), which show good agreement with the data. (Left inset) Zoom of early-time behavior, showing initially slow growth for dikes with decreasing tip pressure. (Right inset) Closeup of the chamber pressure versus dike length.

$\mathcal{T}$	$\dot{a}^* \times 10^{-2}$	$t^* \times 10^3$	$a^* \times 10^0$	$\tilde{t}_{\text{start}} \times 10^5$
-10	3.394	3.135	1.064	2.711
-12	3.249	3.277	1.065	26.86
-14	2.908	3.780	1.099	52.00
-20	2.575	4.346	1.120	162.2

Table S2. Computed log model parameters for various values of $\mathcal{T}$. The parameter a^* is insensitive to the tip pressure for the range of $\mathcal{T}$ studied. It is unclear whether this trend would continue as $\mathcal{T}$ is further decreased. As expected, the starting time of the logarithmic growth regime, $\tilde{t}_{\text{start}}$, increases as the tip pressure decreases.

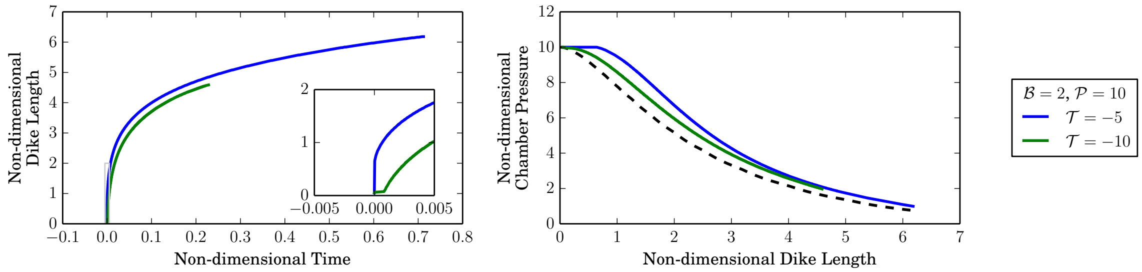

Figure S5. Dike length versus time and chamber pressure versus dike length with $\mathcal{K} = 3$, $\mathcal{B} = 2$, $\mathcal{P} = 10$, for $\mathcal{T} = -5$ and $\mathcal{T} = -10$. In contrast to that with $\mathcal{T} = -10$, the case with $\mathcal{T} = -5$ initially experienced unstable crack growth, growing to approximately 0.64 times the chamber radius.

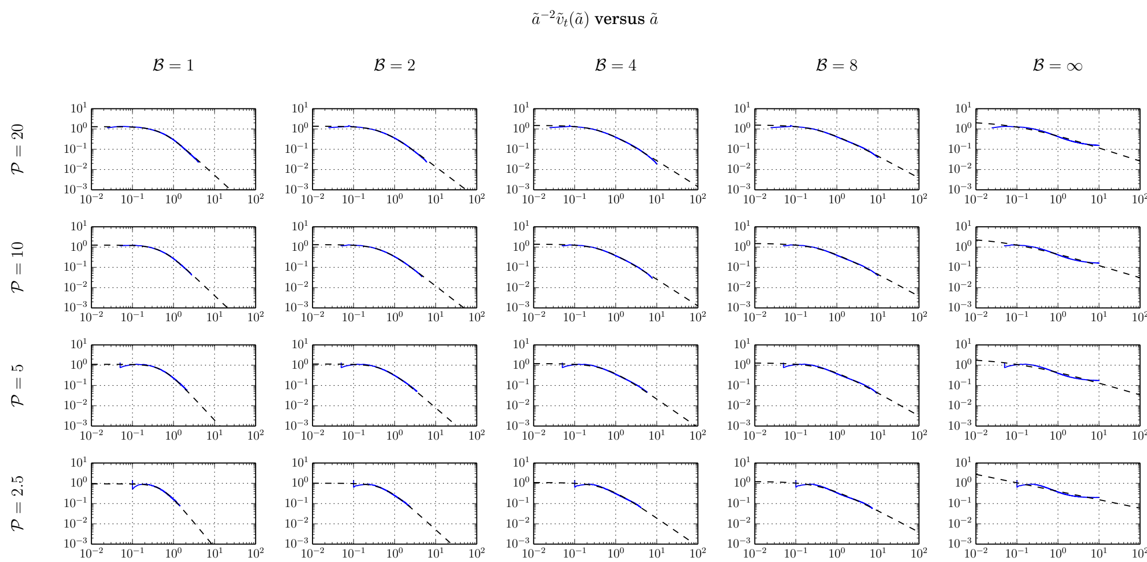

Figure S6. Tip cavity volume plotted against dike length over the explored parameter space. The numerical results are shown with blue lines, while the best fit of the functional form (8) is shown with dashed black lines. The model does not approximate well the cases with $\mathcal{B} = \infty$, which appear to have a limiting behavior $\tilde{v}_t(\tilde{a}) \sim \tilde{a}^2$ for $\tilde{a}/A^* \gg 1$.

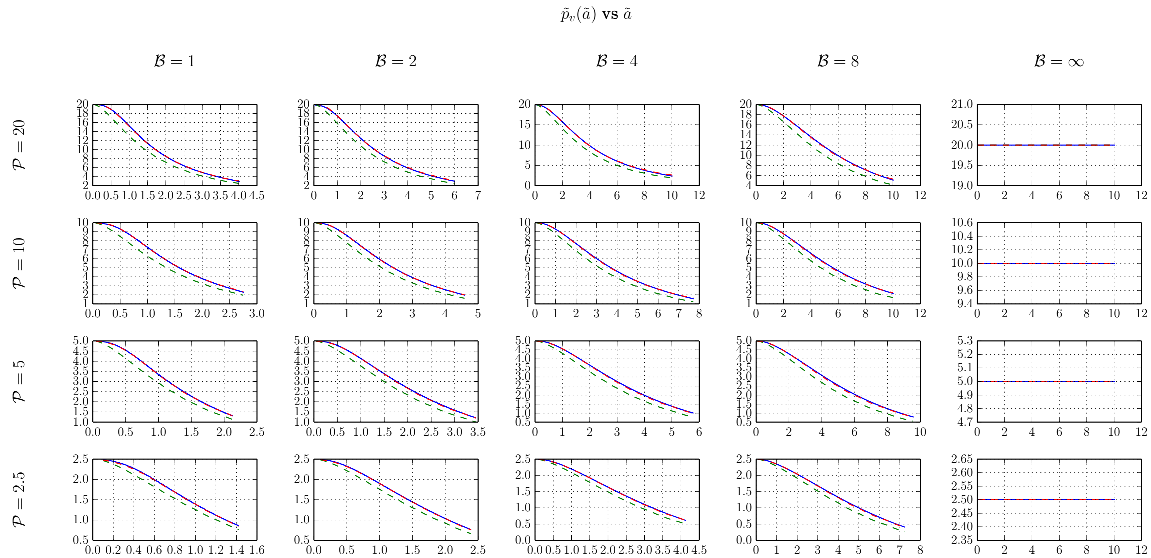

Figure S7. Chamber pressure versus length over the explored parameter space. Shown are the numerical results (blue solid lines), the model (6) (green dashed lines), and the refined model (7) with previously computed best fit $\tilde{v}_t(\tilde{a})$ (red dashed lines).